Influence of Cross Sectional Geometry on Surface Plasmon Polariton Propagation in Gold Nanowires

Scott Nauert,[†] Aniruddha Paul,[†] Yu-Rong Zhen,[‡] David Solis, Jr.,[§] Leonid Vigderman,[†] Wei-Shun Chang,[†] Eugene R. Zubarev,[†] Peter Nordlander,[‡,§] and Stephan Link[†,§,*]

[†]Department of Chemistry, [‡]Department of Physics and Astronomy, and [§]Department of Electrical and Computer Engineering, Laboratory for Nanophotonics, Rice University, Houston, Texas 77005, United States

ABSTRACT We investigated the effects of cross sectional geometry on surface plasmon polariton propagation in gold nanowires (NWs) using bleach-imaged plasmon propagation and electromagnetic simulations. Chemically synthesized NWs have pentagonally twinned crystal structures, but recent advances in synthesis have made it possible to amplify this pentagonal shape to yield NWs with a five-pointed-star cross section and sharp end tips. We found experimentally that NWs with a five-pointed-star cross section, referred to as SNWs, had a shorter propagation length for surface plasmon polaritons at 785 nm, but a higher effective incoupling efficiency compared to smooth NWs with a pentagonal cross section, labeled as PNWs. Electromagnetic simulations revealed that the electric fields were localized at the sharp ridges of the SNWs, leading to higher absorptive losses and hence shorter propagation lengths compared to PNWs. On the other hand, scattering losses were found to be relatively uncorrelated with cross sectional geometry, but were strongly dependent on the plasmon mode excited. Our results provide insight into the shape-dependent waveguiding properties of chemically synthesized metal NWs and the mode-dependent loss mechanisms that govern surface plasmon polariton propagation.

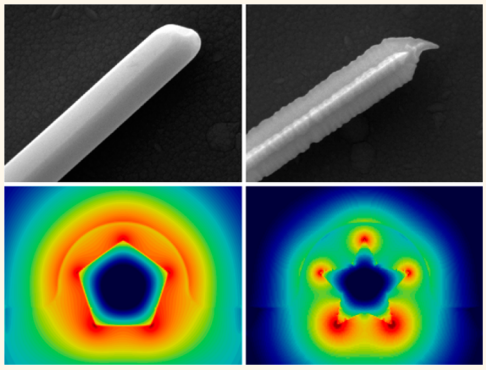

KEYWORDS: gold nanowires · surface plasmon polaritons · plasmon propagation · plasmonic waveguides · cross sectional geometry

A major challenge in the quest for smaller optical devices is to overcome the diffraction limit, which determines the smallest possible lateral dimension for dielectric optical components. One-dimensional metallic structures are promising candidates as basic components in nanoscale optical devices due to their ability to confine light to subwavelength dimensions in the form of surface plasmon polaritons (SPPs), which are collective oscillations of the conduction band electrons propagating at a metal–dielectric interface.[1−6] Metallic nanowires (NWs) and stripes with diameters smaller than ~200 nm have been of particular interest for subwavelength waveguiding and have become attractive candidates for various plasmonic applications, such as optical interconnects and routers in plasmonic circuits,[7−10] as plasmonic logic gates,[11,12] and as Fabry–Perot resonators.[13−16] Furthermore, NWs show great promise as a sensing platform for remote-excitation surface-enhanced Raman scattering.[17−19] However, SPP propagation in metallic NWs suffers significant losses at optical frequencies through both radiative (scattering) and nonradiative (Joule heating) pathways, limiting the SPP propagation length to a few tens of micrometers.[7,8,13,14,20] Understanding the parameters that determine these losses and quantifying them in a systematic way is therefore important for the development of low-loss nanoscale devices based on metallic NWs as well as for advancing other continuous plasmonic structures.

Chemically prepared silver[7−9,11−13,20−29] and gold[20,29−34] NWs have been studied extensively with respect to their optical and SPP waveguiding properties because of their high degree of crystallinity and smooth surfaces, which significantly reduce scattering losses and hence lead to longer SPP propagation lengths compared to plasmonic structures fabricated by metal

* Address correspondence to slink@rice.edu.

Received for review October 4, 2013 and accepted December 5, 2013.

Published online December 05, 2013
10.1021/nn405183r

evaporation.[13,22,35] Silver NWs are in general better plasmonic waveguides than gold NWs due to lower intrinsic absorptive losses, especially at optical frequencies where interband transitions in gold contribute to the nonradiative decay of SPPs.[36] However, gold has the advantage that it is chemically more stable than silver, and the difference in SPP propagation lengths becomes less significant at near-infrared frequencies. In addition to the type of metal, the SPP propagation length also depends on the NW diameter, as most clearly demonstrated through calculations.[27,29,37,38] For the fundamental waveguide mode, SPP losses depend inversely on the NW diameter, leading to increased propagation lengths as the diameter increases. In contrast, for higher order SPP modes the behavior is more complex. For some modes, the propagation length can actually increase with decreasing NW diameter and surpass the fundamental mode, giving rise to a less confined, long-range SPP mode.[27,39] Higher order SPP modes with long propagation lengths have recently been identified in chemically prepared gold NWs, where the fundamental mode was strongly quenched due to a lossy dye environment.[31]

Not only the diameter of the NW but also the cross sectional shape matters for SPP propagation.[27,38,39] For NWs with large diameters and cross sectional shapes that contain sharp corners (squares, rectangles, pentagons, *etc.*), the SPPs are localized at the sides and corners.[39] As the diameter is reduced, side modes are no longer supported and the corner modes start to hybridize into collective modes with mode profiles determined by the symmetry of the cross sectional shape.[27,39] An underlying substrate, as is usually present in experiments, furthermore modifies the overall symmetry of the system and leads to additional mixing of the supported SPP modes.[27,38] For the smallest diameter, the hybridized modes yield a strongly confined fundamental SPP mode that is similar to the one of a perfectly circular wire.[38] Because of this convergence chemically prepared silver and gold NWs with a pentagonal cross section and small (~100 nm) diameters could be successfully modeled assuming a cylindrical shape. However, recent theoretical calculations comparing substrate-supported NWs having polygonal cross sections with sharp corners to cylindrical NWs have found that the propagation length is longest in cylindrical NWs due to the minimized interaction with the substrate, as a cylinder makes only a line contact with a surface.[38]

Our understanding of the dependence of SPP propagation on NW cross sectional shape has so far mainly been inferred from simulations.[38,39] However, the recent chemical synthesis of gold NWs with different cross sections[40,41] has now opened up the possibility of studying experimentally the effects of NW geometry on SPP propagation. In the present study, we addressed the effect of NW cross sectional geometry on waveguiding properties by measuring SPP propagation lengths at an excitation wavelength of 785 nm in chemically synthesized NWs with pentagonal and five-pointed-star cross sections, labeled here as PNWs and SNWs. Our experimental approach relied on imaging SPP propagation through a far-field fluorescence-based technique known as bleach-imaged plasmon propagation (BIIPP),[30,31,42,43] where the plasmonic near-field is mapped by exploiting the photobleaching of nearby fluorescent dye molecules. The results were compared with full-wave electromagnetic simulations, which both supported our experimental results and also helped to explain the difference in SPP propagation lengths measured for PNWs and SNWs. In particular, these calculations allowed us to investigate how the cross section and SPP mode number influence absorptive and radiative losses.

RESULTS AND DISCUSSION

Gold PNWs and SNWs were characterized by scanning electron microscopy (SEM) as shown in Figure 1. The images in the insets are highlighting the tip morphology and cross sectional shape of the two types of NWs. Both PNWs and SNWs had pentagonally twinned crystal structures. The major differences between these gold NWs were their tip shape and cross sectional geometry. The PNWs had five smooth side facets and rounded tips (Figure 1A), while the corners of SNWs were elongated into ridges, giving SNWs a five-pointed-star-shaped cross section that tapered

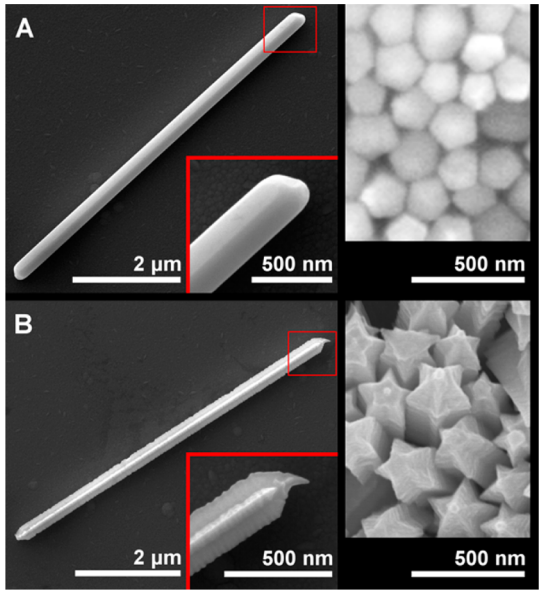

Figure 1. SEM images of chemically synthesized gold NWs with pentagonal and five-pointed star cross sections. (A) Image of a PNW. (B) SEM image of an SNW illustrating the sharp ridges along the NW length. Insets show the top view of vertically standing NWs clearly demonstrating their pentagonal and five-pointed-star cross sections, respectively.

down to a sharp tip (Figure 1B). SNWs and PNWs had comparable dimensions, measuring 5−7 μm in length and averaging 330 ± 40 nm and 390 ± 60 nm in diameter, respectively. The difference in the average diameter of the NWs was comparable to their respective standard deviations (see also Figure S1). This small diameter difference is therefore not expected to significantly affect SPP propagation. The diameter for both PNWs and SNWs was taken to be the diameter of the smallest circle encompassing the NW (*i.e.*, outer diameter).

SPP propagation lengths were measured at 785 nm using BIIPP to elucidate the effect of morphological differences between the two types of NWs. The results of representative BIIPP experiments are shown in Figure 2. Details of the sample preparation and analysis are given in the Methods section. Briefly, NWs were deposited onto a glass coverslip, and a 90 nm thin layer of poly(methyl methacrylate) (PMMA) was spin-coated onto the NWs to create a spacer layer, on top of which a dye (cardiogreen) was spin-coated to form a ~5 nm fluorescent film.[31] All measurements were carried out on a home-built sample scanning fluorescence microscope.

The BIIPP experiments involved three main steps. A sample scanned fluorescence image was first recorded

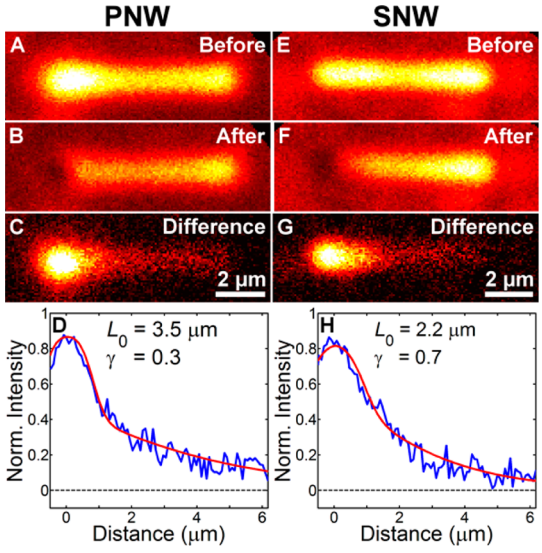

Figure 2. Visualizing SPP propagation for a PNW (left column) and an SNW (right column). (A) Fluorescence image of a PNW recorded at an excitation power of 0.06 μW. (B) Fluorescence image of the same NW recorded after 10 min of exposure of the left NW end to 1.6 μW of 785 nm laser light, which induced dye photobleaching. (C) Difference image obtained by subtracting B from A. The difference image represents the fluorescence intensity lost due to photobleaching by direct laser excitation and through near-field interactions of the dye molecules with the propagating SPPs. (D) Width-averaged intensity line section (blue) taken along the NW axis and normalized to the initial NW fluorescence intensity. Fit (red) to eq 1 yielded an SPP propagation length of L = 3.5 μm and an effective incoupling efficiency of γ = 0.3. (E−H) Same as A−D for an SNW. The fit in H gave an SPP propagation length of L = 2.2 μm and an effective incoupling efficiency of γ = 0.7.

with 785 nm excitation using a low, nondamaging power of 0.06 μW, as shown for a PNW in Figure 2A. At an optimized spacer layer thickness, the dye fluorescence was enhanced for areas on top of the NWs by a factor of about 4−5 times compared to the background fluorescence from the continuous dye film due to plasmon-exciton interactions.[44−46] After recording this initial image, the left end of the NW was positioned using a piezo scanning stage so that it was excited by the focused laser beam at an increased laser power of 1.6 μW for 10 min. In the final step, a second fluorescence image was taken of the same NW at the initial low laser power (Figure 2B). During the high-power exposure in the second step, the SPP near-field photobleached the cardiogreen dye molecules along the NW. The amount of photobleaching depends on the local electric field, exposure time, and the intensity of the laser excitation.[30,31,42] A permanent map of the SPP propagation was then obtained by constructing the difference image, Figure 2C, by subtracting the image after photobleaching (Figure 2B) from the one recorded before (Figure 2A). A width-averaged intensity line section along the long NW axis was extracted from the difference image and illustrates the decay of the propagating SPP (Figure 2D). The same experimental procedure was followed for SNWs, and the results of a representative BIIPP experiment for an individual SNW are shown in Figure 2E−H. In all cases, the 785 nm laser was circularly polarized because the irregular and different tip morphologies lead to efficient mixing of the different polarization components and the excitation of both m = 0 and m = 1 modes.[25,45]

Propagation lengths of L = 3.5 μm and L = 2.2 μm for the PNWs and SNWs, respectively, were extracted from the bleach intensity line sections shown in Figure 2D,H. These line sections as obtained from the difference images in Figure 2C,G were fit to a kinetic rate model for dye photobleaching given by

$$I_{\text{bleach}} = \eta\left(1 - \exp\left(-kI_{G,0}t\exp\left(-\frac{x^2}{2\sigma^2}\right) - kI_{SPP,0}t\exp\left(-\frac{x}{L}\right)\right)\right) \quad (1)$$

where t is time, x is the spatial coordinate along the NW, σ describes the width of the Gaussian laser beam, k is the photobleaching rate constant, and $I_{G,0}$ and $I_{SPP,0}$ are the intensities of the laser and the SPP near-field at the point of excitation (*i.e.*, x = 0). Equation 1 accounts for dye photobleaching due to direct Gaussian laser excitation and for photobleaching from the exponentially decaying SPP near-field along the NW. η < 1.0 describes an effective maximum bleach intensity, and its derivation is shown in the Supporting Information.[43]

The two pre-exponential factors $kI_{G,0}$ and $kI_{SPP,0}$ in eq 1 can be used to estimate an effective incoupling efficiency γ of the laser light into the SPP modes of the NW. The incoupling efficiency is defined as the ratio of

light intensity coupled to SPP modes and the incident laser intensity at the point of excitation, $\gamma = I_{SPP,0}/I_{G,0}$. Figure 2D,H gives $\gamma = 0.3$ for the PNW and $\gamma = 0.7$ for the SNW. The results from Figure 2 suggest that the difference in SPP propagation length and effective incoupling efficiency between the NWs is related to their morphology.

The distributions of the propagation length and effective incoupling efficiency indeed confirm the conclusion that PNWs had a longer propagation length than SNWs, but the latter had a higher effective incoupling efficiency (Figure 3). As can be seen in Figure 3A, the average propagation length of $\langle L \rangle$ = 3.0 μm for the PNWs was about 1 μm longer than the value of $\langle L \rangle$ = 1.8 μm obtained for SNWs. This reduction in SPP propagation is assigned to their unique cross sectional geometry, as will be investigated in more detail below using finite difference time domain (FDTD) calculations. On the other hand, the average incoupling efficiency was higher for SNWs ($\langle \gamma \rangle$ = 0.63) than for PNWs ($\langle \gamma \rangle$ = 0.48), as can be seen from the distributions in Figure 3B. We performed a two-sample *t* test to assess the significance of this conclusion and found that results are statistically significant at the p = 0.01 level. The increased effective incoupling efficiency for the SNWs can be explained by the sharp tip and larger surface roughness at the NW end compared to PNWs (see insets of Figure 1), leading to better momentum matching of the SPPs with the free space photons.[25,46]

To better understand how the NW cross sectional geometry affects SPP losses, FDTD calculations were performed to determine the propagation lengths and electric field (E-field) distributions of the PNWs and SNWs excited at 785 nm (Figure 4). Figure 4A,D shows the cross sectional NW geometry and dielectric environment used to mimic the experimental BlIPP conditions for a PNW and an SNW, respectively. The NWs were positioned on a glass substrate and were surrounded by a PMMA spacer layer, which was index matched to the glass using a refractive index of n = 1.5. The PMMA spacer layer was covered by a thin dye layer, which was surrounded by air. The dye layer was modeled as a lossy medium, as our recent study showed that absorptive damping by the dye layer can selectively quench specific SPP modes, thus affecting the measurement of the SPP propagation length in BlIPP.[31] As shown in Figure S2, with the inclusion of the PMMA spacer layer, only negligible changes of the SPP propagation length were caused by the dye film. The SNWs were modeled with an ideal five-pointed-star cross section with an inner diameter half that of the outer diameter, and PNWs were modeled with an ideal pentagonal cross section. PNWs have often been approximated as having a circular cross section in several previous studies,[25,26,29−31,47] and we show in the Supporting Information, Figures S5−S7, that this

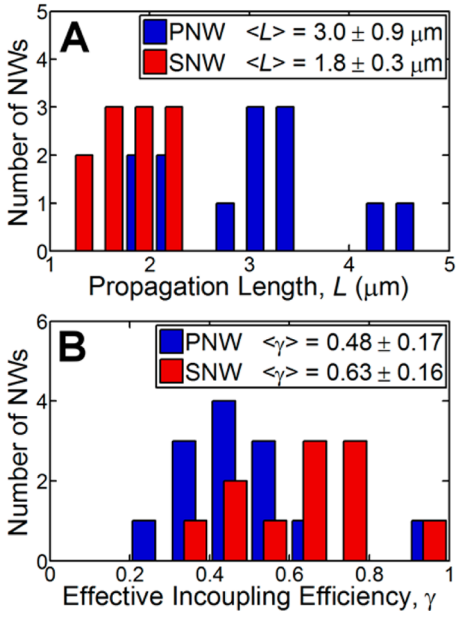

Figure 3. (A) Histogram of propagation lengths obtained from BlIPP measurements of 13 PNWs and 11 SNWs. (B) Histogram of effective incoupling efficiencies for the same NWs.

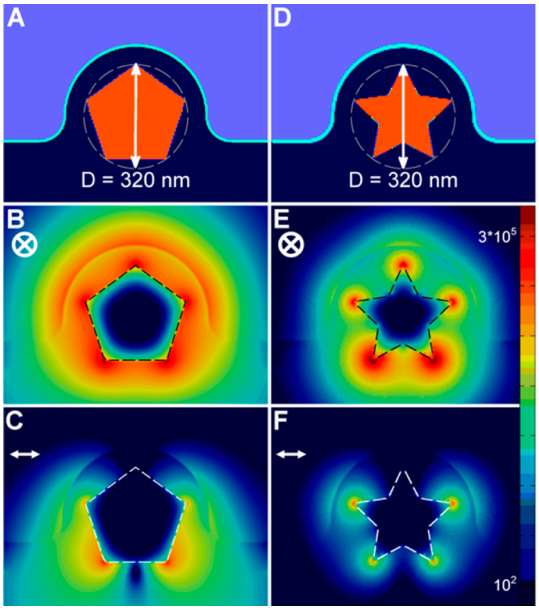

Figure 4. Electromagnetic calculations for a PNW (left column) and an SNW (right column). (A) Schematic illustrating the cross sectional PNW geometry and dielectric environment surrounding the PNW used in the FDTD calculations. The NW was positioned on a glass substrate and was surrounded by a 50 nm thick PMMA spacer layer, which was index matched to the glass. The PMMA film was coated with a 10 nm thin dye layer, which was exposed to air. (B, C) Cross sectional view of the E-field intensity distribution for the PNW upon longitudinal (B) and transverse (C) polarized laser excitation. (D−F) Same as A−C for an SNW.

approximation introduces slight differences, but is in general justified for the NW diameters studied here. In the simulations the NWs were excited at one end *via* a Gaussian laser beam, and the E-field intensity distributions were calculated along the NWs. Figure 4

shows E-field intensity plots for both NWs upon excitation with 785 nm light of longitudinal (Figure 4B,E) and transverse (Figure 4C,F) polarization. While the E-field was more evenly distributed around the perimeter of the PNW, the simulations established a strong localization of the E-field at the sharp ridges of the SNW. For longitudinal polarized excitation, the maximum E-field intensity at the ridges of the SNW was three times higher than the maximum intensity surrounding the PNW, while the maximum intensity was comparable for the PNW and SNW with transverse polarization. As shown in more detail below, this difference in the E-field intensity pattern is directly linked to the differences in SPP propagation length (Figure 5).

The propagation lengths calculated by FDTD and shown in Figure 5 are in good agreement with the experimental results and support the conclusion of a shorter propagation length for the SNWs compared to the PNWs. Figure 5A,B illustrates the decay of the E-field intensity as a function of NW length for both longitudinal (red) and transverse (blue) polarized excitation of a PNW and an SNW, respectively. Fitting of the E-field intensity profiles to exponentials yielded SPP propagation lengths of $L_{\parallel} = 3.2\ \mu$m (longitudinal polarized excitation) and $L_{\perp} = 3.1\ \mu$m (transverse polarized excitation) for the PNW, while the propagation lengths for the SNWs of $L_{\parallel} = 0.9\ \mu$m and $L_{\perp} = 0.7\ \mu$m were significantly shorter. To compare the calculated

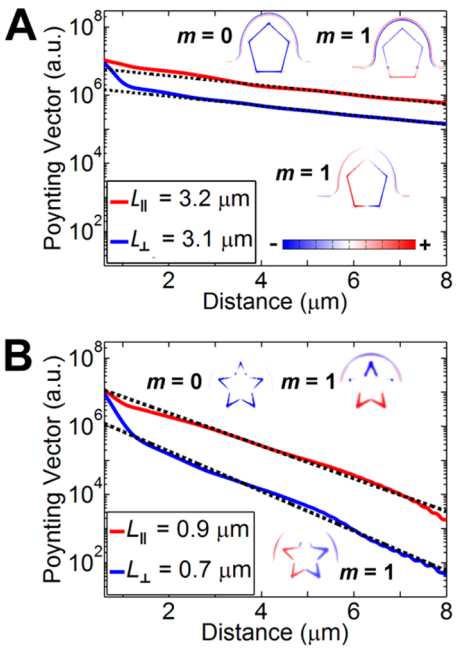

Figure 5. SPP propagation lengths obtained from FDTD calculations. (A) Semilog plot of the Poynting vector along the main axis of a PNW for longitudinal and transverse polarized excitation. Charge plots are given in the insets. The propagation lengths obtained from fitting the decay profiles were $L_{\parallel} = 3.2\ \mu$m and $L_{\perp} = 3.1\ \mu$m, respectively. (B) Same as A for an SNW. The propagation lengths for longitudinal and transverse polarized excitation were $L_{\parallel} = 0.9\ \mu$m and $L_{\perp} = 0.7\ \mu$m, respectively.

propagation lengths to the experimentally determined values, which were acquired using circular polarized excitation, $L_{\parallel}$ and $L_{\perp}$ were averaged. In the case of the PNW we obtain very good agreement between the FDTD simulations and the experimental results. The trend of a longer propagation length compared to the SNWs was also well reproduced. The calculated SPP propagation length was more than a factor of 3 larger for the PNWs compared to the SNWs.

Additional simulations of the propagation length for SNWs as a function of NW diameter, shown in Figure S2, illustrate that the propagation length increased by less than a factor of 2 when the SNW outer diameter (smallest circle encompassing the SNW) was doubled so that the SNW inner diameter (largest circle enclosed by the SNW) now matched the (outer) diameter of the PNWs. Differences in NW diameter and the convention used for the NW diameter therefore could not explain the difference in SPP propagation length. The E-field intensity distributions in Figure 4 furthermore show that the propagating modes were localized at the NW−medium interface, justifying the convention of using the outer NW diameter in our analysis. The value calculated for the SNWs was slightly underestimated, most likely due to meshing error at the SNW ridges compared with the actual morphology of experimental SNWs, which had ridges with a radius of curvature of approximately 2 nm. Surface roughness in the case of the experimental SNWs could also be important, but should then lead to an overestimation of the calculated *vs* measured propagation lengths. The FDTD simulations, which modeled PNWs and SNWs with the same surface roughness, artificially introduced by the finite grid spacing, confirm that the cross sectional shape played the dominant role in the reduction of the propagation length for the SNWs.

Charge plots (insets to Figure 5) reveal that longitudinally polarized light led to the excitation of a mixed mode with nearly equal contributions from the $m = 0$ and $m = 1$ modes, while transversely polarized light resulted in the excitation of only the $m = 1$ mode in both types of NWs. Experimentally using circular polarized excitation, both $m = 0$ and $m = 1$ were excited. To understand the relationship between the E-field intensity distributions, propagation lengths, and the cross sectional shapes of the NWs, we next consider the different loss mechanisms that contribute to the damping of propagating SPPs in NWs and in particular their relative contributions.

The two main loss mechanisms for SPP propagation are absorptive losses (Joule heating), which are proportional to the E-field intensity inside the metal, $|E|^2$, and radiative (scattering) losses, which are proportional to the square of the net dipole moment of the oscillating charge set up in the NW upon SPP excitation.[48] Although absorptive losses lead to heating of the metal NW, this heating cannot be responsible for the

exponential decay observed in BlIPP, as shown in Figure S4. For both NWs, the E-field intensity cross sections in Figure 4 suggest that longitudinal excitation gave rise to larger absorptive losses than transverse excitation due to the larger E-fields inside the metal. In addition, transverse polarized excitation resulted in an E-field intensity distribution that had a node in the middle of the NW, further reducing the total E-field intensity inside the NW. When comparing the two types of NWs, it is apparent that the E-field intensity in the interior of the NWs was larger in the SNWs, particularly inside the ridges. Thus, the larger absorptive losses are a major factor responsible for the shorter SPP propagation length in the SNWs. However, calculations determining the relative strength of absorptive and scattering losses for different modes are necessary before a firm conclusion regarding the origin of the difference in propagation length can be drawn.

Power flow calculations excluding the impact of the surrounding dielectric environment were performed to obtain a quantitative picture of the magnitude for absorptive *vs* scattering losses and to determine the intrinsic dependence of these two loss mechanisms on the modes and cross sectional shape. These power flow calculations were performed using the finite element method (FEM) because for NWs in a vacuum the effect of NW shape on absorption and scattering losses could be more accurately modeled with FEM compared to FDTD simulations. Both types of NWs with lengths of 6 μm and diameters of 320 nm were placed in a vacuum so that longitudinal polarized excitation led to a pure m = 0 mode and transverse polarized excitation led to a pure m = 1 mode. For these FEM simulations, the NWs were excited at one end by a Gaussian laser beam, and power flow calculations were carried out within a cylindrical observation volume that measured 400 nm in length and had a radius of 600 nm (Figure 6A). SPP attenuation due to absorption and scattering losses was then calculated for both types of NWs and m = 0 and m = 1 modes by exploiting energy conservation, *i.e.*, $P_{in} = P_{out} + P_{scat} + P_{abs}$. Figure 6B displays the propagation losses for the different NWs and SPP modes as percentages of P_{abs} and P_{scat} relative to the power entering the observation volume P_{in}.

Power flow calculations for pure m = 0 and m = 1 modes in these NWs reveal that scattering losses were relatively independent of NW cross sectional shape. Figure 6B shows that the m = 1 mode had more than a 5-fold increase in scattering losses over the m = 0 mode for both NWs, indicating a strong correlation between scattering loss and SPP mode number. This result is in agreement with a recent study, which found that for silver PNWs with a diameter larger than 300 nm the fundamental SPP mode remains strongly confined, while higher order modes leak by radiative losses into the substrate.[27] Although scattering losses, especially

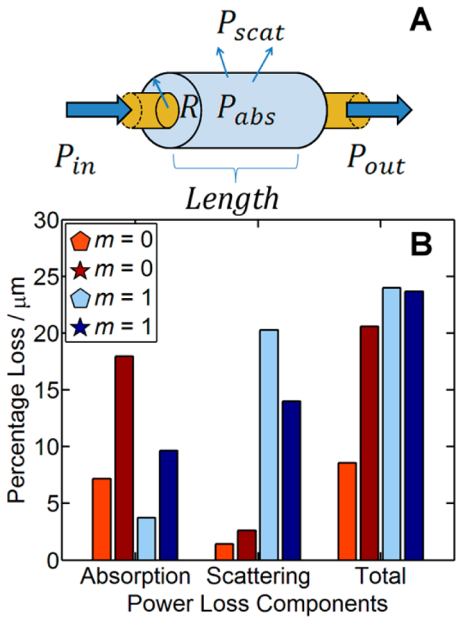

Figure 6. (A) Schematic illustrating the observation volume (light blue) used to monitor the power flow in the calculations. The observation volume had a length of 400 nm and a radius of 600 nm. Absorption and scattering losses were calculated using $P_{in} = P_{out} + P_{scat} + P_{abs}$, which ensures that the total power was conserved. (B) Power attenuation for PNWs and SNWs and m = 0 and m = 1 modes. Attenuation was expressed as a percentage of power lost due to absorption and scattering relative to the power entering the observation volume.

due to the leaky m = 1 modes, contributed significantly to the overall losses, there is no clear correlation between NW cross sectional geometry and scattering losses, considering that both m = 0 and m = 1 modes were excited.

The above analysis clearly shows that the main reason for the shorter propagation length of the SNWs is the difference in absorptive losses. Figure 6B reconfirms the conclusion of larger absorptive losses for SNWs inferred from the results in Figure 4. The absorptive losses in SNWs were about 2.5 times as large as in the PNWs for both the m = 0 and m = 1 modes. Therefore, the main effect of the cross sectional geometry on SPP propagation was that the localized E-fields at the sharp ridges led to higher absorptive losses and therefore shorter propagation lengths in SNWs as compared to PNWs.

CONCLUSIONS

We have measured SPP propagation lengths and effective incoupling efficiencies in NWs with pentagonal and five-pointed-star cross section at 785 nm using BlIPP. Our experimental results show that the effective incoupling efficiency was higher for the SNWs than PNWs due to their sharper tips and rougher surfaces, which increased the probability to meet the momentum matching criterion required to optically launch SPPs. FDTD calculations supported the longer propagation lengths determined by BlIPP for the PNWs

compared to SNWs. The simulated E-field intensity distributions revealed that the E-fields were almost evenly distributed around the PNWs, while they were concentrated around the sharp ridges for the NWs with a five-pointed-star cross section. The high local concentration of the E-field intensity at these ridges resulted in larger fields inside the metal NW and hence larger absorptive losses. This result was also confirmed by power flow calculations that quantified the contribution of absorptive and scattering losses for different NW cross sections and SPP modes. This analysis showed that both scattering and absorptive losses were dependent on the SPP mode number, while absorptive losses were also shape dependent and higher for NWs with a five-pointed-star cross section. Our results not only provide important new insight into the shape-dependent waveguiding properties of chemically synthesized metal NWs but also shed light on the different loss mechanisms involved in surface plasmon polariton propagation.

METHODS

Sample Preparation. Purified pentahedrally twinned gold NWs stabilized by cetyltrimethylamonium bromide (CTAB) and synthesized by following a previously published procedure[49] were used as seed particles for the synthesis of both PNWs and SNWs. PNWs used in this study were grown from these precursors by fast overgrowth, while SNWs were grown from the same NW precursors in the presence of silver nitrate, as described in detail by Vigderman *et al.*[40] The lengths and diameters of both types of NWs were characterized by SEM using a JEOL 6500F SEM. The PNWs measured 6.1 $\pm$ 1.2 μm in length and 390 $\pm$ 60 nm in diameter, while the SNWs measured 6.3 $\pm$ 1.2 μm in length with inner diameters of 180 $\pm$ 20 nm and outer diameters of 330 $\pm$ 40 nm. For the SNWs, the inner diameter was taken to be the diameter of the largest circle completely covered by the NW, while the outer diameter was taken to be the diameter of the smallest circle completely encompassing the NW. Glass coverslips were cleaned by sonication in Milli-Q water and acetone followed by exposure to an oxygen plasma (Harrick Plasma Cleaner) for 1 min. NW solutions were diluted with Milli-Q water to an appropriate concentration, and 5 μL drops were casted onto the glass coverslips. After drying, the coverslips were washed with ethanol to remove excess CTAB and dried under a low flow of nitrogen. Next, 1 mL of a 4% solution of PMMA (495 kg/mol) in anisole (MicroChem) was spin coated (Headway Research Inc.) at 1000 rpm for 45 s on top of the NWs to deposit a PMMA spacer layer. The samples were respun at 1000 rpm for 45 s and dried for 20 min, after which 30 μL of cardiogreen dye (Sigma Aldrich) in methanol with a concentration of 0.5 mg/mL (6.5×10^{-4} mol L^{-1}) was spin coated onto the samples at 4000 rpm for 40 s. The spacer layer thickness was estimated to be 90 nm using calibration curves for the PMMA thickness provided by MicroChem, while dye layer thickness was previously determined to be 5 nm under these preparation conditions.[31] The uniformity of the PMMA spacer layer was confirmed using atomic force microscopy as shown in Figure S3.

BIIPP Measurements. BIIPP measurements were conducted using an inverted microscope setup (Axiovert 200) equipped with a piezoelectric scanning stage (Physik Instrumente) connected to a surface probe controller (RHK Technology). Light from a 785 nm diode laser (Power Technology Inc.) focused through a 50$\times$ air-spaced objective (Zeiss) with a numerical aperture of 0.8 was used as the excitation source to take sample-scanned fluorescence images as well as to photobleach the cardiogreen dye on top of the NWs. Fluorescence from the sample passed through appropriate dichroic and notch filters to remove reflected laser light and was collected by an avalanche photodiode detector (Perkin-Elmer). The optical resolution was ~350 nm (fwhm) and was measured by taking scattering images of 25 $\times$ 86 nm gold nanorods. Sample scanned fluorescence images were taken of 10 $\times$ 10 μm areas with a resolution of 128 $\times$ 128 pixels and an integration time of 10 ms/pixel. The excitation power was typically 0.02$-$0.12 μW, while a higher laser exposure power of 1.6 μW was employed for the photobleaching step.

The image acquisition and analysis method utilized in BIIPP has been detailed in previous reports.[30,42] To summarize, an initial fluorescence image of a NW sample was taken at a low excitation power. Next, the laser was focused on one end of the NW, and the NW was irradiated at a higher power to photobleach the dye molecules on top of the NW end and along the path of SPP propagation. Photobleaching was suspended typically after 1, 3, 5, 10, and 20 min of laser exposure at a power of 1.6 μW to retake an image of the sample at the original low excitation power. An image shift correction and background correction were applied to each image taken after the high power laser exposure to account for minor sample and focus drift as well as any small fluctuations in the excitation power. After each exposure period, a difference image was created by subtracting the corrected images taken just after photobleaching from the first image taken prior to any photobleaching using a MATLAB (v. R2010b) program. Each difference image represents the cumulative amount of photobleaching due to laser exposure and SPP propagation along the NW for the given exposure time. These difference images were used to extract the SPP propagation length and effective incoupling efficiency for individual NWs. To find the SPP propagation length and effective incoupling efficiency for each NW, the difference image was first rotated to lie along the *x*-axis, and then a 3-pixel width-averaged intensity line section was taken along the length of the NW. The SPP propagation length and effective incoupling efficiency were determined by fitting the width-averaged intensity line section to the kinetic rate model for dye photobleaching given in eq 1. By acquiring a time series of difference images, the determination of the SPP propagation length and effective incoupling efficiency can be significantly improved by globally fitting the corresponding photobleach intensity line sections. The parameter σ describing the spatial extent of direct dye photobleaching by the Gaussian laser profile was determined by bleaching the dye film in the background away from the NWs. A value of $\sigma = 0.5-0.7$ μm was used for all BIIPP experiments, which is in agreement with the optical resolution given by a fwhm of 350 nm.

Electromagnetic Calculations. Electromagnetic simulations were carried out using the FDTD method and the finite element method. The FDTD method was used for the simulations in Figures 4 and 5, as it is better suited to modeling the complex substrate, spacer layer, dye layer, and air environments surrounding the NWs while maintaining a small enough mesh size. For FDTD simulations (Lumerical), both the NWs were placed on a glass substrate and were coated with a 50 nm thick dielectric spacer layer with a refractive index of n = 1.5 to simulate the PMMA film, as shown in Figure 4A,E. The NWs were modeled as semi-infinite long structures with one end inside the computational domain and the other end using a perfectly matched layer to minimize reflections and mimic the semi-infinite NW length. The PNW cross section was modeled as an ideal regular pentagon, and the SNW was modeled with a five-pointed-star cross section with an inner diameter around the base of the star ridges 0.5 time as large as the outer diameter around the tips of the star ridges. The meshing process used a 4 nm $\times$ 4 nm grid spacing in the cross sectional plane, introducing some artificial surface roughness to the NWs. Tabulated values for the dielectric function of gold by Johnson and Christy were used for the NWs.[50] The PMMA spacer layer was covered with a 10 nm

absorptive dye layer with a complex refractive index of $n = 1.54 + 0.36i$[31] and exposed to air with a refractive index of $n = 1.0$. The refractive index of the dye was calculated assuming an oscillator strength for the optical absorption of the dye of 0.1. A Gaussian beam with a wavelength of 785 nm was normally incident on the substrate and focused on the ends of the NWs. SPP propagation lengths for different NWs and polarizations were determined from linear fits to semilog plots of the time-averaged energy flow (Poynting vector) along the NW length as a function of distance.

Finite element method simulations were carried out for the same excitation conditions using COMSOL Multiphysics. The NWs were modeled using the same NW cross sectional geometry as employed for the FDTD calculations but assumed to have a length of 6 μm and an outer diameter of 320 nm and were placed in a vacuum. While inapplicable for simulations of semi-infinite long NWs, FEM was used instead of FDTD for power loss calculations in a finite NW section because FEM is better suited to modeling the exact NW geometry in the absence of a complex dielectric environment. A cylindrical observation volume 400 nm long and with a radius of 600 nm was defined along the NW in the power flow calculations. A large radius for the observation volume was used to minimize boundary effects for these power flow calculations. Absorption and scattering losses were calculated exploiting the energy conservation $P_{in} = P_{out} + P_{scat} + P_{abs}$, where P_{in} is the power flow into the observation volume through the NW, P_{out} is the power flow out of the observation volume through the NW, P_{scat} is the power flow out of the observation volume not occurring through the NW, and P_{abs} is the remaining power unaccounted for by P_{out} and P_{scat}.

Conflict of Interest: The authors declare no competing financial interest.

Acknowledgment. This work was funded by the Robert A. Welch Foundation (C-1664, C-1222), ONR (N00014-10-1-0989), ARO (MURI W911NF-12-1-0407), and NSF (CHE-0955286). D.S. was supported by an NSF Graduate Research Fellowship grant (no. 0940902). E.R.Z. acknowledges financial support by NSF (DMR-1105878). This work was supported in part by the Data Analysis and Visualization Cyberinfrastructure funded by the NSF under grant OCI-0959097. We acknowledge Yumin Wang for his kindly help with FEM calculations.

Supporting Information Available: This document contains information regarding NW diameter characterization and its influence on SPP propagation, the effect of the dye film on SPP propagation, characterization of the spacer layer thickness, the effect of nanowire heating, comparison of plasmon propagation in nanowires with circular and pentagonal cross sections, and details of the BIIPP model. This material is available free of charge *via* the Internet at http://pubs.acs.org.

REFERENCES AND NOTES

1. Brongersma, M. L.; Shalaev, V. M. The Case for Plasmonics. *Science* **2010**, *328*, 440–441.
2. Takahara, J.; Yamagishi, S.; Taki, H.; Morimoto, A.; Kobayashi, T. Guiding of a One-Dimensional Optical Beam with Nanometer Diameter. *Opt. Lett.* **1997**, *22*, 475–477.
3. Dickson, R. M.; Lyon, L. A. Unidirectional Plasmon Propagation in Metallic Nanowires. *J. Phys. Chem. B* **2000**, *104*, 6095–6098.
4. Barnes, W. L.; Dereux, A.; Ebbesen, T. W. Surface Plasmon Subwavelength Optics. *Nature* **2003**, *424*, 824–830.
5. Ozbay, E. Plasmonics: Merging Photonics and Electronics at Nanoscale Dimensions. *Science* **2006**, *311*, 189–193.
6. Gramotnev, D. K.; Bozhevolnyi, S. I. Plasmonics beyond the Diffraction Limit. *Nat. Photonics* **2010**, *4*, 83–91.
7. Sanders, A. W.; Routenberg, D. A.; Wiley, B. J.; Xia, Y. N.; Dufresne, E. R.; Reed, M. A. Observation of Plasmon Propagation, Redirection, and Fan-out in Silver Nanowires. *Nano Lett.* **2006**, *6*, 1822–1826.
8. Yan, R.; Pausauskie, P.; Huang, J.; Yang, P. Direct Photonic–Plasmonic Coupling and Routing in Single Nanowires. *Proc. Natl. Acad. Sci. U.S.A.* **2009**, *106*, 21045–21050.
9. Fang, Y. R.; Li, Z. P.; Huang, Y. Z.; Zhang, S. P.; Nordlander, P.; Halas, N. J.; Xu, H. X. Branched Silver Nanowires as Controllable Plasmon Routers. *Nano Lett.* **2010**, *10*, 1950–1954.
10. Charbonneau, R.; Lahoud, N.; Mattiussi, G.; Berini, P. Demonstration of Integrated Optics Elements Based on Long-Ranging Surface Plasmon Polaritons. *Opt. Express* **2005**, *13*, 977–984.
11. Wei, H.; Li, Z. P.; Tian, X. R.; Wang, Z. X.; Cong, F. Z.; Liu, N.; Zhang, S. P.; Nordlander, P.; Halas, N. J.; Xu, H. X. Quantum Dot-Based Local Field Imaging Reveals Plasmon-Based Interferometric Logic in Silver Nanowire Networks. *Nano Lett.* **2011**, *11*, 471–475.
12. Wei, H.; Wang, Z.; Tian, X.; Kall, M.; Xu, H. Cascaded Logic Gates in Nanophotonic Plasmon Networks. *Nat. Commun.* **2011**, *2*, 387.
13. Ditlbacher, H.; Hohenau, A.; Wagner, D.; Kreibig, U.; Rogers, M.; Hofer, F.; Aussenegg, F. R.; Krenn, J. R. Silver Nanowires as Surface Plasmon Resonators. *Phys. Rev. Lett.* **2005**, *95*, 257403.
14. Allione, M.; Temnov, V. V.; Fedutik, Y.; Woggon, U.; Artemyev, M. V. Surface Plasmon Mediated Interference Phenomena in Low-Q Silver Nanowire Cavities. *Nano Lett.* **2008**, *8*, 31–35.
15. Dorfmuller, J.; Vogelgesang, R.; Weitz, R. T.; Rockstuhl, C.; Etrich, C.; Pertsch, T.; Lederer, F.; Kern, K. Fabry-Perot Resonances in One-Dimensional Plasmonic Nanostructures. *Nano Lett.* **2009**, *9*, 2372–2377.
16. Wiley, B. J.; Lipomi, D. J.; Bao, J. M.; Capasso, F.; Whitesides, G. M. Fabrication of Surface Plasmon Resonators by Nanoskiving Single-Crystalline Gold Microplates. *Nano Lett.* **2008**, *8*, 3023–3028.
17. Fang, Y.; Wei, H.; Hao, F.; Nordlander, P.; Xu, H. Remote-Excitation Surface-Enhanced Raman Scattering Using Propagating Ag Nanowire Plasmons. *Nano Lett.* **2009**, *9*, 2049–2053.
18. Lee, S. J.; Moskovits, M. Remote Sensing by Plasmonic Transport. *J. Am. Chem. Soc.* **2012**, *134*, 11384–11387.
19. Hutchison, J. A.; Centeno, S. P.; Odaka, H.; Fukumura, H.; Hofkens, J.; Uji-i, H. Subdiffraction Limited, Remote Excitation of Surface Enhanced Raman Scattering. *Nano Lett.* **2009**, *9*, 995–1001.
20. Kusar, P.; Gruber, C.; Hohenau, A.; Krenn, J. R. Measurement and Reduction of Damping in Plasmonic Nanowires. *Nano Lett.* **2012**, *12*, 661–665.
21. Akimov, A. V.; Mukherjee, A.; Yu, C. L.; Chang, D. E.; Zibrov, A. S.; Hemmer, P. R.; Park, H.; Lukin, M. D. Generation of Single Optical Plasmons in Metallic Nanowires Coupled to Quantum Dots. *Nature* **2007**, *450*, 402–406.
22. Knight, M. W.; Grady, N. K.; Bardhan, R.; Hao, F.; Nordlander, P.; Halas, N. J. Nanoparticle-Mediated Coupling of Light into a Nanowire. *Nano Lett.* **2007**, *7*, 2346–2350.
23. Staleva, H.; Skrabalak, S. E.; Carey, C. R.; Kosel, T.; Xia, Y. N.; Hartland, G. V. Coupling to Light, and Transport and Dissipation of Energy in Silver Nanowires. *Phys. Chem. Chem. Phys.* **2009**, *11*, 5889–5896.
24. Guo, G. P.; Yang, R.; Ren, X. F.; Wang, L. L.; Shi, H. Y.; Hu, B.; Yu, S. H.; Guo, G. C. Excitation of Surface Plasmons in a Single Silver Nanowire Using Higher-Order-Mode Light. *Phys. E* **2010**, *42*, 1751–1754.
25. Li, Z. P.; Bao, K.; Fang, Y. R.; Huang, Y. Z.; Nordlander, P.; Xu, H. X. Correlation between Incident and Emission Polarization in Nanowire Surface Plasmon Waveguides. *Nano Lett.* **2010**, *10*, 1831–1835.
26. Shegai, T.; Miljkovic, V. D.; Bao, K.; Xu, H. X.; Nordlander, P.; Johansson, P.; Kall, M. Unidirectional Broadband Light Emission from Supported Plasmonic Nanowires. *Nano Lett.* **2011**, *11*, 706–711.
27. Song, M. X.; Bouhelier, A.; Bramant, P.; Sharma, J.; Dujardin, E.; Zhang, D. G.; Colas-des-Francs, G. Imaging Symmetry-Selected Corner Plasmon Modes in Penta-Twinned Crystalline Ag Nanowires. *ACS Nano* **2011**, *5*, 5874–5880.
28. Zhang, S.; Wei, H.; Bao, K.; Håkanson, U.; Halas, N. J.; Nordlander, P.; Xu, H. Chiral Surface Plasmon Polaritons on Metallic Nanowires. *Phys. Rev. Lett.* **2011**, *107*, 096801.

29. Wild, B.; Cao, L.; Sun, Y.; Khanal, B. P.; Zubarev, E. R.; Gray, S. K.; Scherer, N. F.; Pelton, M. Propagation Lengths and Group Velocities of Plasmons in Chemically Synthesized Gold and Silver Nanowires. *ACS Nano* **2012**, *6*, 472–482.
30. Solis, D.; Chang, W.-S.; Khanal, B. P.; Bao, K.; Nordlander, P.; Zubarev, E. R.; Link, S. Bleach-Imaged Plasmon Propagation (Blipp) in Single Gold Nanowires. *Nano Lett.* **2010**, *10*, 3482–3485.
31. Paul, A.; Solis, D.; Bao, K.; Chang, W.-S.; Nauert, S.; Vidgerman, L.; Zubarev, E. R.; Nordlander, P.; Link, S. Identification of Higher Order Long-Propagation-Length Surface Plasmon Polariton Modes in Chemically Prepared Gold Nanowires. *ACS Nano* **2012**, *6*, 8105–8113.
32. Ben, X.; Park, H. S. Strain Engineering Enhancement of Surface Plasmon Polariton Propagation Lengths for Gold Nanowires. *Appl. Phys. Lett.* **2013**, *102*.
33. Neubrech, F.; Pucci, A.; Cornelius, T. W.; Karim, S.; García-Etxarri, A.; Aizpurua, J. Resonant Plasmonic and Vibrational Coupling in a Tailored Nanoantenna for Infrared Detection. *Phys. Rev. Lett.* **2008**, *101*, 157403.
34. Blythe, K. L.; Mayer, K. M.; Weber, M. L.; Willets, K. A. Ground State Depletion Microscopy for Imaging Interactions between Gold Nanowires and Fluorophore-Labeled Ligands. *Phys. Chem. Chem. Phys.* **2013**, *15*, 4136–4145.
35. Critchley, K.; Khanal, B. P.; Górzny, M. Ł.; Vigderman, L.; Evans, S. D.; Zubarev, E. R.; Kotov, N. A. Near-Bulk Conductivity of Gold Nanowires as Nanoscale Interconnects and the Role of Atomically Smooth Interface. *Adv. Mater.* **2010**, *22*, 2338–2342.
36. Raether, H. *Surface Plasmons on Smooth and Rough Surfaces and on Gratings*; Springer: New York, 1988.
37. Wang, Y.; Ma, Y.; Guo, X.; Tong, L. Single-Mode Plasmonic Waveguiding Properties of Metal Nanowires with Dielectric Substrates. *Opt. Express* **2012**, *20*, 19006–19015.
38. Zhang, S.; Xu, H. Optimizing Substrate-Mediated Plasmon Coupling toward High-Performance Plasmonic Nanowire Waveguides. *ACS Nano* **2012**, *6*, 8128–8135.
39. Jung, J.; Søndergaard, T.; Bozhevolnyi, S. I. Theoretical Analysis of Square Surface Plasmon-Polariton Waveguides for Long-Range Polarization-Independent Waveguiding. *Phys. Rev. B* **2007**, *76*, 035434.
40. Vigderman, L.; Zubarev, E. R. Starfruit-Shaped Gold Nanorods and Nanowires: Synthesis and Sers Characterization. *Langmuir* **2012**, *28*, 9034–9040.
41. Anderson, L. J. E.; Zhen, Y.-R.; Payne, C. M.; Nordlander, P.; Hafner, J. H. Gold Nanobelts as High Confinement Plasmonic Waveguides. *Nano Lett.* **2013**, ASAP.
42. Solis, D.; Willingham, B.; Nauert, S. L.; Slaughter, L. S.; Olson, J.; Swanglap, P.; Paul, A.; Chang, W.-S.; Link, S. Electromagnetic Energy Transport in Nanoparticle Chains *via* Dark Plasmon Modes. *Nano Lett.* **2012**, *12*, 1349–1353.
43. Solis, D.; Paul, A.; Chang, W. S.; Link, S. Mechanistic Study of Bleach-Imaged Plasmon Propagation (Blipp). *J. Phys. Chem. B* **2013**, *117*, 4611–4617.
44. Anger, P.; Bharadwaj, P.; Novotny, L. Enhancement and Quenching of Single-Molecule Fluorescence. *Phys. Rev. Lett.* **2006**, *96*, 113002.
45. Chen, Y.; Munechika, K.; Ginger, D. S. Dependence of Fluorescence Intensity on the Spectral Overlap between Fluorophores and Plasmon Resonant Single Silver Nanoparticles. *Nano Lett.* **2007**, *7*, 690–696.
46. Kinkhabwala, A.; Yu, Z. F.; Fan, S. H.; Avlasevich, Y.; Mullen, K.; Moerner, W. E. Large Single-Molecule Fluorescence Enhancements Produced by a Bowtie Nanoantenna. *Nat. Photonics* **2009**, *3*, 654–657.
47. Kenens, B.; Rybachuk, M.; Hofkens, J.; Uji-i, H. Silver Nanowires Terminated by Metallic Nanoparticles as Effective Plasmonic Antennas. *J. Phys. Chem. C* **2012**, *117*, 2547–2553.
48. Roder, P. B.; Pauzauskie, P. J.; Davis, E. J. Nanowire Heating by Optical Electromagnetic Irradiation. *Langmuir* **2012**, *28*, 16177–16185.
49. Khanal, B. P.; Zubarev, E. R. Purification of High Aspect Ratio Gold Nanorods: Complete Removal of Platelets. *J. Am. Chem. Soc.* **2008**, *130*, 12634–12635.
50. Johnson, P. B.; Christy, R. W. Optical Constants of the Noble Metals. *Phys. Rev. B* **1972**, *6*, 4370–4379.